First magnetic seismology of the CME reconnection outflow layer in the low corona with 2.5-D MHD simulations of the Kelvin-Helmholtz instability

Katariina Nykyri[1] and Claire Foullon[2]

Received 21 June 2013; revised 27 July 2013; accepted 30 July 2013; published 23 August 2013.

[1] For conditions observed in the low corona, we perform 2.5-D magnetohydrodynamic (MHD) simulations of the Kelvin-Helmholtz instability (KHI) at the surface of a coronal mass ejection (CME). We match the observed time development of the KHI with simulated growth from 110 MHD experiments representing a parametric range of realistic magnetic field strengths and orientations and two key values of the velocity shear, ΔV, inferred from observations. The results are field strengths $B_e \approx$ 8–9 G and $B_s \approx$ 10–11 G in the CME reconnection outflow layer and the surrounding sheath, respectively, for $\Delta V \approx 770\,\mathrm{km\,s^{-1}}$; for nearly perpendicular orientation (1° tilt) of $\mathbf{B_s}$ with respect to the flow plane, $\mathbf{B_e}$ can be tilted between 3 and 10°; tilting $\mathbf{B_s}$ up to 15° would slow the growth of the KHI by too much. Our simulations also reveal hidden dynamics and structure of the CME ejecta layer such as plasma mixing via reconnection in the vortices. **Citation:** Nykyri, K., and C. Foullon (2013), First magnetic seismology of the CME reconnection outflow layer in the low corona with 2.5-D MHD simulations of the Kelvin-Helmholtz instability, *Geophys. Res. Lett.*, *40*, 4154–4159, doi:10.1002/grl.50807.

1. Introduction

[2] As a coronal mass ejection (CME) propagates from the Sun to the Earth, its kinematics and hence its geoeffectiveness depend on the total drag force it experiences. *Foullon et al.* [2011] showed the first clear imaged observations of the temporally and spatially resolved evolution of the Kelvin-Helmholtz Instability (KHI) at the flank of a CME in the low corona. The phenomenon is well-known at the interface of a shocked solar wind flow and a planetary magnetosphere of the Earth and other planets. At Earth, numerical simulation studies have shown that the nonlinear KH waves can produce significant mass transport from the solar wind into the Earth's magnetotail with diffusion coefficients of order $10^9 \mathrm{m^2\,s^{-1}}$ both via magnetic reconnection [*Nykyri and Otto*, 2001] and ion diffusion [*Cowee et al.*, 2010]. The presence of KH vortices in the CME is thus expected to produce plasma mixing and diffusion which can affect the drag forces [*Foullon et al.*, 2011]. Therefore, understanding the plasma and magnetic field conditions when the KHI can develop in the CME is important for terrestrial space weather.

[3] *Foullon et al.* [2013] have recently performed a detailed imaging and spectral study of the event of 3 November 2010, allowing a determination of several critical properties of the KHI and the shear flow interface between the surrounding corona and the CME ejecta identified as a reconnection outflow layer. These include plasma temperatures and densities, magnitude of the shear flow (ΔV), lag time of the first KH perturbations since onset conditions (t_0) and the KH wavelength, period and linear growth rate. However, the magnetic field (B-field, hereafter) is more difficult to ascertain. Through coronal seismology, waves supported by structures in the corona have been a means to probe the local B-field conditions in those structures [e.g., *Verwichte et al.*, 2009]. In a similar fashion, our purpose is to indirectly determine the range of possible B-field strengths and orientations in the CME reconnection outflow layer and surrounding coronal sheath by matching the observations with 2.5-D magnetohydrodynamic (MHD) simulations of a velocity shear driven KHI. Freely varying parameters are the B-field strength and orientation on both sides of the shear flow boundary.

2. Methodology

[4] The KHI study is conducted with a 2.5-D MHD model explained in detail in *Otto and Fairfield* [2000]. This model is utilized in several studies of the KHI [*Nykyri and Otto*, 2001; *Nykyri et al.*, 2006; *Taylor et al.*, 2008]. Figure 1a shows an image of a CME observed with the Atmospheric Imaging Assembly (AIA) aboard the Solar Dynamics Observatory (SDO) and reproduced from *Foullon et al.* [2011], showing KHI waves at the northern flank of the CME. The simulation box corresponds approximately to a rectangular box in Figure 1a. The simulation geometry with a coordinate system is described in Figure 1b, where the ejecta layer magnetic field, $\mathbf{B_1}$, is rotated by φ_1 and the surrounding coronal field, $\mathbf{B_2}$, by φ_2 about the y axis from the perpendicular direction (z direction) with respect to the flow plane (hereafter, we refer to the ejecta layer (surrounding sheath) parameters with subindex 1 (2)). The hot ejecta plasma (orange) is moving into $-x$ direction. The y axis is perpendicular to the initial current layer separating the ejecta and coronal plasma. The simulations use a hyperbolic tangent profile for the shear flow layer with thickness $L_0 = 1$ Mm. Because the most prominent KH waves are observed when the CME size is ~100 Mm (see Figure 2), we choose this x scale for our simulations. The $[x, y]$ system size is $100 \times 60 L_0$ in an adjustable grid with 489×289 grid points, with a maximum resolution

[1]Department of Physical Sciences, Embry-Riddle Aeronautical University, Daytona Beach, Florida, USA.
[2]College of Engineering, Mathematics and Physical Sciences, University of Exeter, Exeter, UK.

Corresponding author: K. Nykyri, Department of Physical Sciences, Embry-Riddle Aeronautical University, Daytona Beach, FL 32114, USA. (nykyrik@erau.edu)

0094-8276/13/10.1002/grl.50807

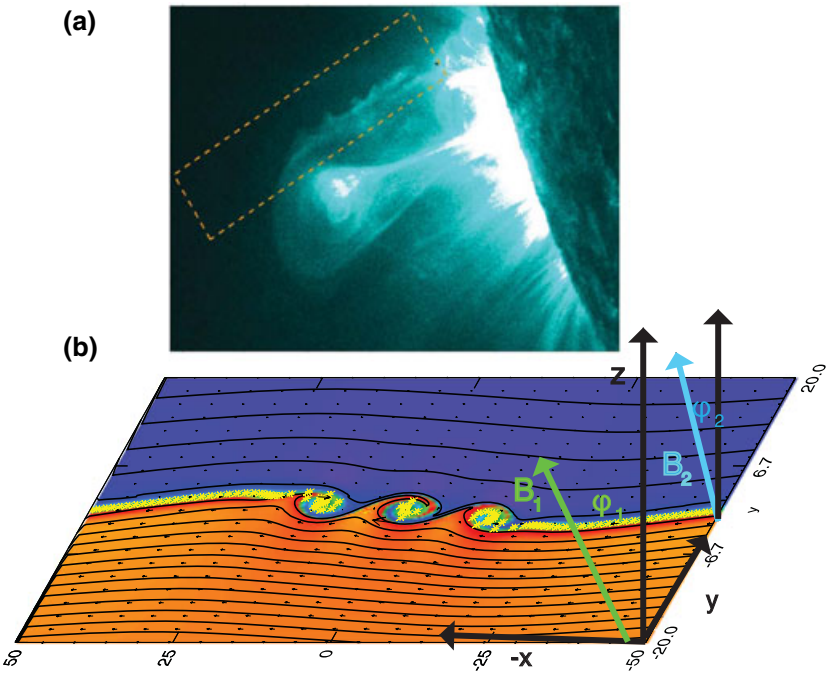

Figure 1. Geometry of the simulation: (a) SDO/AIA 131Å image of CME erupting from the Sun, with the KH waves visible on its northern flank (reproduced from *Foullon et al.* [2011] by permission of the AAS); (b) simulation plane, coordinate system and B-field orientation in ejecta layer ($\mathbf{B_1}$) and surrounding corona ($\mathbf{B_2}$). Plasma temperature, magnetic field lines and vectors projected onto simulation plane are shown. This simulation plane corresponds approximately to the rectangular box in Figure 1a.

of 0.05 (50 km) around the shear flow layer. The simulations use periodic (reflective) boundary conditions in x (y) and use a frame moving with half of ΔV making the KH ripples approximately stationary. Initial density, pressure, and velocity are chosen according to values reported in *Foullon et al.*[2013, Tables 2 and 3]. These are the plasma electron densities $n_1 = n_2 = 7.1 \times 10^8$ cm^{-3} and the electron temperatures, $T_{e1} = 11.6$ MK and $T_{e2} = 4.5$ MK. We assume the plasma to be in thermal equilibrium ($T_i = T_e$). The plasma pressure at both sides of the boundary is computed from $P = n_e k_B T_e + n_i k_b T_i = 2 n_e k_B T_e$, resulting in $P_1 = 0.227$ Pa and $P_2 = 0.088$ Pa. ΔV inferred from the observations is

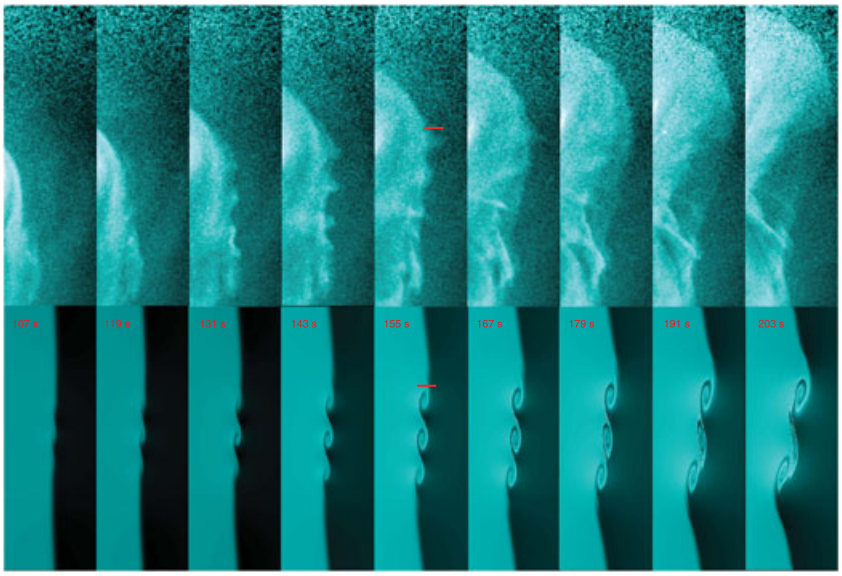

Figure 2. Time evolution of KH waves (top) in snapshots taken every 12 s as observed by SDO/AIA in 131Å on the CME flank region in Figure 1a (reproduced from *Foullon et al.* [2011] by permission of the AAS) and (bottom) in SDO instrument response to simulated temperature and density for Case 4c (with $\varphi_1 = 3°$). In each snapshot, the horizontal scale is 40 Mm and the vertical scale is (Figure 2, top) from 30 to 180 Mm above the solar surface and (Figure 2, bottom) 100 Mm, comoving with the KHI. The horizontal red line at 155 s depicts the maximum scale size of one of the observed structures.

Table 1. Simulation Cases[a]

Case	B_2 (G)	B_1 (G)	φ_2 (°)	φ_1 (°)	ΔV (km s^{-1})	β_2	β_1
1a	8.0	5.4	1	0–90	680	0.35	1.97
2a	9.0	6.8	1	0–90	680	0.27	1.25
3a	10.0	8.1	1	0–90	680	0.22	0.86
4a	11.0	9.3	1	0–90	680	0.18	0.66
5a	12.0	10.0	1	0–90	680	0.15	0.52
3b	10.0	8.1	10	0–90	680	0.22	0.86
2c	9.0	6.8	1	0–20	772	0.27	1.25
3c	10.0	8.1	1	0–15	772	0.22	0.86
4c	**11.0**	**9.3**	**1**	0–15	**772**	**0.18**	**0.66**
5c	12.0	10.0	1	0–15	772	0.15	0.52
4d	11.0	9.3	15	0–15	772	0.18	0.66

[a]Benchmark is presented in bold.

680 ± 92 km s^{-1}. The time in each simulation is normalized to Alfvén wave travel time through the scale length, L_0, using the Alfvén speed, V_A, in the sheath. The simulations use current dependent resistivity ($\eta(J)$) model 1 from *Nykyri and Otto* [2001], with model parameters $\kappa = 0.0025$ and $J_C = 1.1B_2/(L_0\mu_0)$, where μ_0 is the permeability of free space. This resistivity model avoids the collapse of current layers to the grid separation and allows for magnetic reconnection. The exact choice of η does not appear to be important for the results as long as it avoids fast large-scale diffusion.

[5] The simulation cases are presented in Table 1. Starting with values of the sheath magnetic field, B_2, we infer the ejecta B-field strength, B_1, from the total pressure balance: $B_1 = \sqrt{2\mu_0(P_2 + {B_2}^2/(2\mu_0) - P_1)}$. In order to narrow down the parameter space, we run at first stage denoted "a", 5 × 14 simulations corresponding to five different B-field values (Cases 1a–5a, such that B_2 = 8, 9, 10, 11, and 12 G, resulting in B_1 = 5.4, 6.8, 8.1, 9.3, and 10 G, respectively), 14 different orientations of the ejecta field (φ_1 = 0, 3, 5, 10, 15, 20, 25, 30, 35, 40, 45, 50, 55, 90) and setting the sheath field orientation to $\varphi_2 = 1°$ and $\Delta V = 680$ km s^{-1}.

[6] The time evolution and growth of the KHI in these simulations are compared to three critical times in the solar observations reported by *Foullon et al.* [2011, 2013]: (1) observation of the first clear KH perturbation $t_1 = 111 \pm 8$ s (second frame in Figure 2, top); (2) the growth at $t_2 = t_1 + 36$ s = 147± 8 s corresponding to the observation of the ripple with maximum scale length normal to the initial shear flow layer (fifth frame); (3) the observed pear-shape of the ejecta at $t_3 = t_2 + 48$ s = 195± 8 s (last frame). At the next stage "b", we repeat all the 14 simulations for B_2 = 10 G, but setting $\varphi_2 = 10°$ (Case 3b). At stage "c", we choose the best cases from stage "a" for follow-up study using $\Delta V = 772$km s^{-1} (B_2 = 9, 10, 11, and 12 G, φ_1 = 0, 3, 5, 10, 15°, and $\varphi_2 = 1°$) (Cases 2c–5c). At final stage "d", we choose the best case from stage "c" corresponding to B_2 = 11 G, but setting $\varphi_2 = 15°$ (Case 4d).

3. Results

3.1. Benchmark Simulation

[7] Figure 2 (bottom) shows nine snapshots from Case 4c, with $\varphi_1 = 3°$, showing the SDO/AIA instrument response [*Lemen et al.*, 2012] to simulated temperature and density taken every 12 s. At 103–119 s (first and second frame) the perturbations of the boundary due to KHI are clearly visible. By 143 s, three KH ripples are clearly visible. By 155 s, one of the KH ripples in the AIA observations reaches a scale length of about 10 Mm indicated by a red horizontal line in Figures 2 (top) and 2 (bottom). In the simulations, this scale length appears to be slightly lower, about 7 Mm, but one can see a lighter intensity halo surrounding the three structures against the darker background making the overall structure of the largest ripple about 10 Mm in the direction normal to the initial velocity shear layer. The subsequent evolution shows the twisting of the KH vortex train and mixing of the plasma within the vortex sheet. The mixing of the plasma is more visible in Figure 3 where the plasma fluid elements (yellow asterisks) initially located at the shear flow boundary get transported into the lower temperature sheath region. This transport takes place via magnetic reconnection occurring in strong current layers generated by the KHI, similar to the phenomena obtained for the Earth's magnetopause simulations [*Nykyri and Otto*, 2001]. By time t_3, the lowest two of the three main vortices are mixed together. The large-scale structure of the KH-unstable surface becomes pear-shaped in reasonable agreement with the AIA observations. Figure 3 indicates that the lighter intensity "halo" (frames 143–203 s in Figure 2) around the main KH ripples correspond to regions of reduced density and magnetic field, resulting in depression in the thermal, magnetic, and total pressure. The mixing of the three vortices into two larger-scale structures at time t_3 is also clearly visible in these density and pressure contours. The initial number of KH ripples is caused by the coexistence of a longer wavelength mode most evident in the first frame of Figure 3c.

[8] Studying the other simulated cases indicates that the pear-shaped structure at t_3 best agrees with observations for very small tilt angles $\varphi_2 = 1°$ and φ_1 = 0–3°. Because the physics of the real CME ejecta is more complicated than can be captured with our 2.5-D simulations, including, for example, acceleration, expansion, and rotation of the CME, we do not require an exact match with the observed large-scale structure but consider this case as a reasonable match. We choose this simulation as our benchmark. For each simulation time frame, we record the maximum value of the velocity perturbation normal to the initial current layer (δv_y) and determine the maximum KH perturbation amplitude, $A_{KH} = \max(\ln(|\delta v_y|))$, as a function of time. Figure 4i shows the time-varying A_{KH}, akin to a growth rate, for the benchmark simulation (red dashed line). A_{KH} values at times 103–119, 155–160, and 200–204 s, corresponding to the three critical times in the benchmark simulation, are indicated by intersection of three color-shaded vertical columns and three horizontal lines. Horizontal and vertical lines are the same in Figures 4a–4k, and they are the references for comparison with the other 109 simulations to narrow down the allowed range of B-field strengths and orientations in the CME ejecta layer and sheath.

3.2. $\Delta V = 680$ km s^{-1}, B_2 = 8–12 G

[9] Figures 4a–4e show A_{KH} as a function of time for Cases 1a–5a, respectively. For each of these cases, $\varphi_2 = 1°$ and 14 simulations with φ_1 = 0 - 90° are presented using solid curves with different colors. The time of the first KH perturbation t_1 is the earliest observation limited by the spatial and temporal resolution of the instrument. Thus, in order to have a reasonable match with the solar observations at time t_1, a time-varying A_{KH} curve should pass above or at the intersection of the horizontal line with the vertical

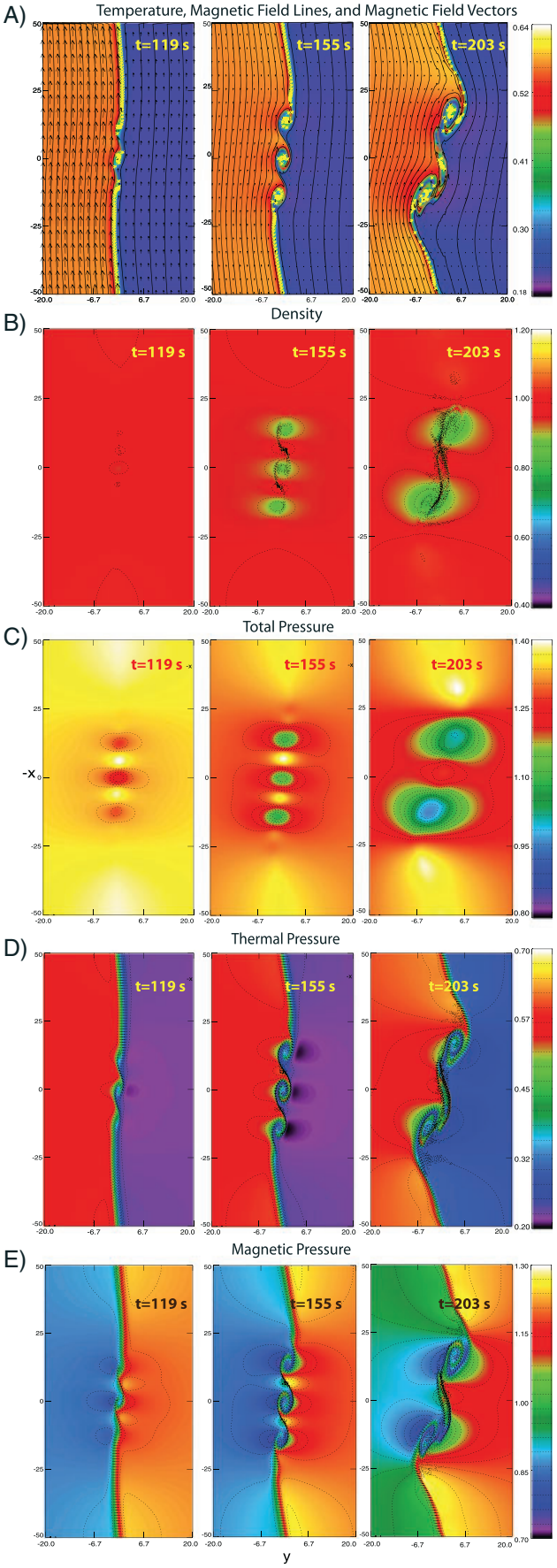

Figure 3

column (highlighted with pale orange color). At time t_1, Case 1a (B_2 = 8 G) yields reasonable growth only for φ_1 = 10° (blue curve); Case 2a (B_2 = 9 G) for φ_1 =5-15°; Case 3a–5a (B_2 = 10, 11, and 12 G) for φ_1 =3–10°. It is interesting to consider why the first KH perturbation occurs sooner for finite tilt angles φ_1 = 3–10° than for fully perpendicular case (φ_1 = 0°). This has to do with an additional initial perturbation perpendicular to the shear layer, which is produced by the increased y component of the $\mathbf{J} \times \mathbf{B}$-force in the MHD momentum equation for finite values of φ_1. Namely, the finite φ_1 results in increased tangential B-field on the ejecta side of the velocity shear layer, which produces an increased z component of the current density $\mathbf{J}$ separating the sheath and ejecta plasma. However, there is a competition between this increased $\mathbf{J} \times \mathbf{B}$-force and stabilization of the KHI for large tangential fields, so that for $\varphi_1 > 15°$ for cases reported in Figures 4c–4e, the growth is less than that for φ_1 = 0°. This feature is further confirmed by simulations presented in Figure 4f (Case 3b). Here $\mathbf{B_2}$ is tilted by φ_2 = 10° instead of 1° making the fastest growth for φ_1 = 0, 3, and 5°. The y component of the $\mathbf{J} \times \mathbf{B}$-force for φ_1 = 10° in Figure 4c (blue) is approximately the same as that for φ_1 = 0° in Figure 4f (black). Note that, simulations by *Miura and Pritchett* [1982] did not include this effect, as they assumed a fully symmetric B-field profile across the shear layer.

[10] In order to have a reasonable match with the SDO observations at time t_2, a time-varying A_{KH} curve should, in addition, pass through the intersection of the horizontal line with the vertical column highlighted with bluish-purple color. Case 3a (B_2 = 10 G) satisfies this condition for φ_1 = 5°. Analysis of the simulations indicates that the large-scale growth at time t_3 for any of these cases does not match well the observed pear-shape in SDO/AIA images at t_3. The inadequate large-scale growth at time t_3 for Case 1–5a and 3b is evident in Figure 4 as all curves are much below the intersection of the vertical and horizontal yellow column. For this reason, we next construct simulations for the upper estimate of ΔV.

3.3. $\Delta V = 772$ km s^{-1}, $B_2 = 9$–12 G

[11] The dashed curves in Figures 4g–4j show A_{KH} as a function of time for Cases 2c–5c, respectively. For all of these cases, φ_2 = 1° and φ_1 = 0–20° for curves in Figure 4g, and φ_1 = 0–15° for curves presented in Figures 4h–4j. The solid lines are for cases with ΔV = 680 km s^{-1} and are replotted for comparison. The dotted-dashed curves in Figure 4k show the runs with φ_2 = 15° and the respective dashed-curves, presented also in Figure 4i, are shown in comparison. Now a reasonable large-scale growth at t_3 is observed for B_2 = 10 and 11 G with φ_1 = 0–10° and for B_2 = 12 G with φ_1 = 0 °. All of the three critical growth times are satisfied for B_2 = 10 G with φ_1 = 3–10°, for B_2 = 11 G with φ_1 = 0–10° and for B_2 = 12 G with φ_1 = 0 °. Considering that

Figure 3. Evolution of the KHI at three critical times for same case as shown in Figure 2 in (a) temperature, (b) density, (c) total, (d) thermal, and (e) magnetic pressure. In Figure 3a, asterisks represent fluid elements located initially at the shear flow boundary; black lines are B-field lines and vectors projected onto simulation plane. In Figures 3b–3e, contours are drawn and color bars are in simulation units.

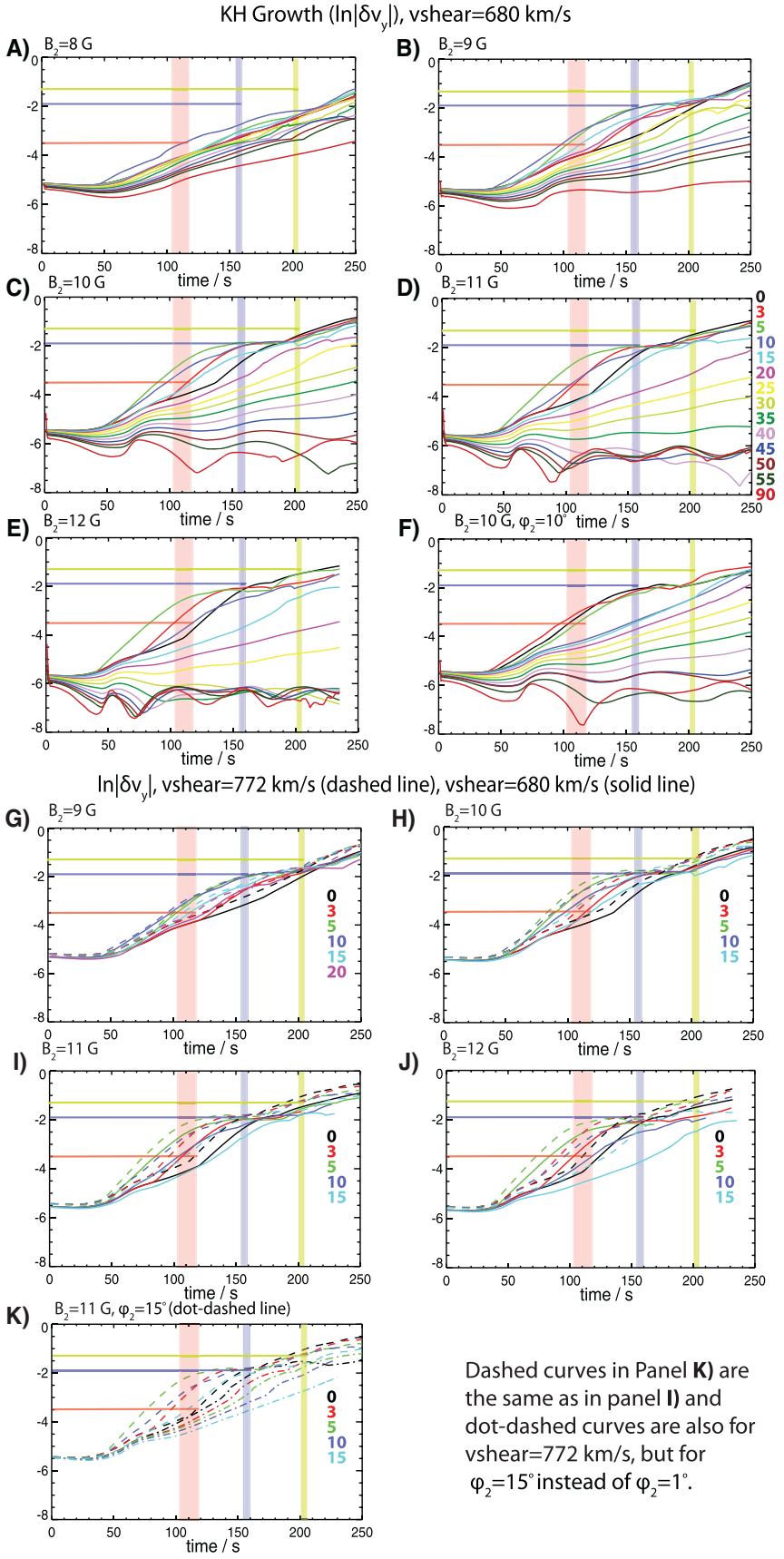

Figure 4. (a–e, g–j)The time evolution of the KH growth (ln $|\delta v_y|$) for Cases 1a–5a (2c–5c), respectively. Different colors correspond to simulations with ejecta field tilted by φ_1 = 0-90°. (f and k) For Case 3b and 4d, respectively. The three vertical columns highlight the three critical times in solar observations.

a configuration where the B-field is exactly perpendicular at either side of the boundary is a singular case, it seems probable that the most favorable conditions for KH growth with the observed plasma parameters occur for $B_2 \approx 10$–11 G and $\varphi_1 \approx 3$–10°. Also, the sheath field needs to be nearly perpendicular ($\varphi_2 \approx 1°$). Increasing φ_2 to 15° (see Figure 4k), will stabilize the KHI for all the values of φ_1 below the observed growth times.

4. Discussion

[12] Our simulations and comparison with the SDO/AIA images of the KHI of 3 November 2010, yield a reasonable match for three critical times if the sheath B-field has strength in the range of $B_2 \approx 10$–11 G and is nearly perpendicular to the flow plane with $\Delta V \approx 770\,\mathrm{km\,s^{-1}}$. The corresponding B-field in the ejecta layer has strength in the range of ≈ 8–9 G and can be tilted by ≈ 3–10° from perpendicular. Our investigation reveals that the B-field orientation is critical for the stabilization of the KHI. Just tilting the sheath field by 15° from perpendicular stabilized the KH significantly below observed growth times for all the ejecta B-field orientations.

[13] Limitations in our method are the 2.5-D system and the assumption of a constant amplitude of the shear flow. The real CME reconnection outflow layer is accelerating and decelerating, probably rotating and expanding, which may result in discrepancy at time t_3 between the large-scale structure observed in SDO/AIA images and the simulations. It is still possible that with ΔV taken as the average value of $680\,\mathrm{km\,s^{-1}}$ inferred from the observations, the sheath B-field values of ∼ 10 G are acceptable solutions. However, by requiring a reasonable match (similar to simulations shown in Figure 2) with the CME pear-shape at t_3, we are quite conservative in our estimation of the allowed B-field and require $\Delta V \approx 770\,\mathrm{km\,s^{-1}}$. Moreover, the KH shape at t_3 is inconsistent with the φ_1 tilt values greater than 10°. It therefore may be possible that in the real CME ejecta layer, the B-field is (i) initially more aligned with the accelerating flow and (ii) as the CME expands the B-field becomes more perpendicular. This evolution in B-field is very probable and is supported by evidence in the observations [*Foullon et al.*, 2013]: (i) The first geometry follows the premise of the field being first a reconnection jet field, therefore, more aligned with the flow. (ii) The second geometry would be an indication that the field lines are still anchored at the Sun as this is the early stage of the eruption in the low corona within a "closed" active region. The field lines would tend to be more horizontal with the surface as the ejecta expands, therefore, perpendicular to the flow.

[14] Our simulations also reveal hidden dynamics and structure of the CME ejecta layer: we observed plasma mixing via reconnection in the vortices and a brighter intensity "halo" in the SDO/AIA instrument response to the simulations, which corresponds to regions with reduced density and B-field resulting in depression of thermal, magnetic and total pressure. The plasma fluid elements were sucked into low pressure centers within the KH vortex. In the real CME, the mixing of plasma in addition to reconnection in the vortices, may happen also via ion diffusion [*Fujimoto and Terasawa*, 1994; *Cowee et al.*, 2010].

[15] The presented results are the first ever indirect determination of the B-field strength and orientation in the CME reconnection outflow layer, and it will be important to expand this study also to other observed KH events for different plasma conditions. For the present conditions, the KH waves are only observed in the 11 MK temperature channel (131Å), and when the plasma betas, β, for 10–11 G (8–9 G) sheath (ejecta) fields are 0.22–0.18 (0.86–0.66) (see Table 1). The compressible effects and magnetic tension forces contribute to the stabilization of the KHI [e.g. *Miura and Pritchett*, 1982]. The best match with the observations is obtained for magnetoacoustic Mach numbers $M_{f,1} = \Delta V/\sqrt{V_A^2 + C_s^2} = 0.81$–0.89 and for Alfvén Mach numbers, along KH wave vector k, $M_{A,k,1} = \frac{\Delta V}{V_{A,k}} = 5.8$–24.8. If the allowed ranges of β, M_f, and $M_{A,k}$ are the determining factors for the KH growth on the CME surface, then the trend in the simulations indicates that events with (i) higher (lower) plasma pressure could favor KHI for higher (lower) B-field strength, and the events with (ii) higher (lower) plasma velocity could favor events with higher (lower) temperature, B-field strength, and tilt angle. Finally the CME size and the coexistence of a longer wavelength mode are determining factors for the finite number of KH ripples.

[16] **Acknowledgments.** K.N.'s work was supported by NSF grant 0847120. C.F. acknowledges financial support from STFC under her Advanced Fellowship ST/I003649/1. The original 2.5-D MHD code was developed by A. Otto. The authors acknowledge the support by the International Space Science Institute (ISSI) and discussions within the ISSI Team 214 on Flow-Driven Instabilities of the Sun-Earth System.

[17] The editor thanks an anonymous reviewer for assistance in evaluating this manuscript.

References

Cowee, M. M., D. Winske, and S. P. Gary (2010), Hybrid simulations of plasma transport by Kelvin-Helmholtz instability at the magnetopause: Density variations and magnetic shear, *J. Geophys. Res.*, *115*, A06214, doi:10.1029/2009JA015011.

Foullon, C., E. Verwichte, V. M. Nakariakov, K. Nykyri, and C. J Farrugia (2011), Magnetic Kelvin-Helmholtz instability at the Sun, *Astrophys. J. Lett.*, *729*, L8, 4 pp., doi:10.1088/2041-8205/729/1/L8.

Foullon, C., E. Verwichte, K. Nykyri, M. J. Aschwanden, and I. G. Hannah (2013), Kelvin-Helmholtz instability of the CME reconnection outflow layer in the low corona, *Astrophys. J.*, *767*, 170, 18 pp., doi:10.1088/0004-637X/767/2/170.

Fujimoto, M., and T. Terasawa (1994), Anomalous ion mixing within an MHD scale Kelvin-Helmholtz vortex, *J. Geophys. Res.*, *99*, 8601–8614

Lemen, J. R., et al. (2012), The Atmospheric Imaging Assembly (AIA) on the Solar Dynamics Observatory (SDO), *Sol. Phys.*, *275*, 17–40, doi:10.1007/s11207-011-9776-8.

Miura, A., and P. L. Pritchett (1982), Nonlocal stability analysis of the MHD Kelvin-Helmholtz instability in a compressible plasma, *J. Geophys. Res.*, *87*, 7431–7444.

Nykyri, K., and A. Otto (2001), Plasma transport at the magnetospheric boundary due to reconnection in Kelvin-Helmholtz vortices, *Geophys. Res. Lett.*, *28*, 3565–3568.

Nykyri, K., A. Otto, B. Lavraud, C. Mouikis, L. Kistler, A. Balogh, and H. Réme (2006), Cluster observations of reconnection due to the Kelvin-Helmholtz instability at the dawn side magnetospheric flank, *Ann. Geophys.*, *24*, 2619–2643.

Otto, A., and D. H. Fairfield (2000), Kelvin-Helmholtz instability at the magnetotail boundary: MHD simulation and comparison with geotail observations, *J. Geophys. Res.*, *105*, 21,175–21,190.

Taylor, M. G. G. T., et al. (2008), The plasma sheet and boundary layers under northward IMF: A multi-point and multi-instrument perspective, *Adv. Space Res.*, *41*, 1619–1629, doi:10.1016/j.asr.2007.10.013.

Verwichte, E., C. Foullon, T. Van Doorsselaere, H. M. Smith, and V. M. Nakariakov (2009), Coronal seismology using transverse loop oscillations, *Plasma Phys. Controlled Fusion*, *51* (12), 124019, 7 pp., doi:10.1088/0741-3335/51/12/124019.